linedepth linedepth

Supporting Information for "Dynamics of episodic magma injection and migration at Yellowstone caldera: revisiting the 2004-2009 episode of caldera uplift with InSAR and GPS data"

Francisco Delgado[1], Raphaël Grandin[1]

[1]Université de Paris, Institut de Physique du Globe de Paris, CNRS, F-75005 Paris, France

Contents of this file

1. Text S1 to S4

2. Figures S1 to S10

Text S1. GPS processing

We use daily position time series processed by the Nevada Geodetic Laboratory (Blewitt et al., 2018) with the JPL GIPSY-OASIS software and a precise point positioning method. These time series are equivalent in quality compared to those used by Wicks et al., (2020) in their study of unrest at Yellowstone between 1996 and 2020. Solutions are referenced to stable North America in the NA12 reference frame (Figure S1), which represents the North America stable interior far from plate boundary effects and post glacial rebound. Since the Yellowstone caldera is located east of the active Basin and Range province, no other geologic processes except for volcano deformation, the post-seismic signal of the 1959 Hebgen Lake earthquake (Puskas et al., 2007), and seasonal processes like surface loading are recorded by the GPS data. We calculate the cumulative displacement of GPS vectors as the difference between the average positions in time windows spanning 10 days before the onset of uplift on July 15 2004, and afterwards on September 1 2009. This way, the GPS data spans the same time interval than the InSAR data. Since the end and start of uplift occurred in the summer, the time-averaged static displacements contain the same amount of seasonal signal, which cancels out when subtracting the total displacements between the two time periods of interest. Puskas et al., (2007) have shown that the velocities calculated by campaign GPS stations during 2000-2003 are almost insensitive to the post-seismic effects of the Hebgen Lake earthquake. Therefore we consider these effects to be negligible with respect to the large magnitude of volcanic unrest in the GPS data.

We also attempted to use the same GPS data but processed by UNAVCO. These time series have more data points between 2000 and 2004 that span the onset of deformation

for the WLWY, LKWY and HVWY stations. However, the horizontal vectors calculated for some stations have different magnitudes than the vectors calculated from the Nevada data. Furthermore, the UNAVCO GPS data provide a worse fit to the two sill model with uniform opening (next section). Therefore, we do not consider this data further.

Text S2. InSAR processing

We use InSAR data acquired by the ENVISAT, ALOS-1 and TerraSAR-X/TanDEM-X satellites. Perpendicular baseline (B_{perp}) plots for all data are shown in Figure S2. Winter C-band and X-band data were not used because interferograms calculated with these images are incoherent.

ENVISAT data

The ENVISAT data span from September 2003 to October 2010. Although there are two ENVISAT IM2 images acquired in September 2003, the large Doppler centroid differences of these images with respect to the rest of the data set precludes estimation of the time series before September 2004. Hence, the InSAR does not have a high enough temporal resolution to resolve the onset of inflation at the caldera floor in September/October 2004. ENVISAT interferograms were processed with the ISTerre NSBAS software (Doin et al., 2011), which is partially based on the JPL ROI_PAC software (Rosen et al., 2004). This processing chain includes a series of corrections that are designed to enhance the coherence of ENVISAT data, including common Doppler centroid filtering, spectral range filtering, geometric coregistration to a master SLC, DEM error corrections, and corrections to atmospheric phase delays prior to phase unwrapping (Doin et al., 2011; Jolivet et al., 2011). Unlike other software, corrections with NSBAS are directly applied on the unfiltered wrapped data.

The topographic phase was removed with the 1 arcsec SRTM DEM. Afterwards, pixels were averaged to 20 looks in azimuth and 4 in range. Interferograms were corrected for atmospheric phase delays with the ERA5 (ECMWF re-analysis) atmospheric model and an empirical function that correlates the phase and the topography on top of the ERA5 corrected interferograms. These corrections were not applied to the IM1 ascending data because they increased the data variance (Figure S3). The relatively low-relief of ∼300 m at Yellowstone implies that most of the atmospheric signals are turbulent and not correlated with the topography, except outside the caldera. Therefore, the ERA-5 correction slightly reduces the variance except for the IM2 descending track because this data set contains the most turbulent atmospheric signals, and these signals cannot be corrected with the ERA-5 model (Figure S3). Empirical atmospheric corrections and range and azimuth ramps were removed directly on the wrapped interferograms and re-estimated with a network-consistent inversion. DEM error corrections (Ducret et al., 2014) were applied only for the IM2 tracks because this correction relies on a heavily redundant interferometric network which is not the case of the IM1 data. Interferograms were filtered with a cascade sliding window algorithm and unwrapped with both the branch and cut (Goldstein et al., 1988) and SNAPHU minimum cost flow algorithms (Chen and Zebker, 2001). In general, coherence is quite good, allowing us to calculate interferograms that span up to two years and with perpendicular baselines (B_{perp}) smaller than 500 m (Figure S2). Interferograms with clear double-bounce signals in areas with wetlands (e.g., Wdowinski and Hong, 2015) introduce sharp phase discontinuities that lead to phase unwrapping errors, even after filtering. Therefore small baseline interferograms with these artifacts were not included in the time series.

ENVISAT time series were calculated with the GIAnT toolbox and the SBAS method (Berardino et al., 2002) for pixels that are coherent in all the selected interferograms (pairs with dashed lines in Figure S2). Prior to time series analysis, interferograms were referenced to a stable non-deforming area (black crosses in Figure 2). We calculate interferograms of total displacement subtracting the first to the last epoch spanning the unrest episode in the reconstructed time series (interferogram hereafter). We prefer this over rate maps of mean velocity because the deformation is non-linear during the episode of uplift. We calculate data uncertainties with the data standard deviation in areas of no deformation. In general the data uncertainty ranges between 0.6 and 0.9 cm for the interferograms, $\sim$20 times lower than the amplitude of the deformation signals. Had we used the grids of mean velocity, the data uncertainty would be even lower because velocity fitting results in a low pass filtering procedure. However, this approach does not consider the non-linearity of the cumulative deformation signal. The noisiest interferogram is from the IM2 descending track because it contains more turbulent atmospheric signals than any of the other three sets.

ERS-1/2 data

We use ERS-1/2 descending data (Figure S4) to qualitatively compare the caldera subsidence during 1992-1995 (Aly and Cochran, 2011; Wicks et al., 1998) and uplift at NGB during 1996-2000 (Wicks et al., 2006) with that of the 2004-2009 unrest. The 1992-1995 data are a stack of two interferograms acquired during 1992-1993 and 1993-1995 and processed with 20 looks in azimuth and 4 in range with a power spectrum filtering strength of 0.5. Ramps were removed from the interferograms prior to stacking. The 1996-2000 interferogram was processed with 40 looks in azimuth and 8 looks in range and with a

power spectrum filtering strength of 0.7 to increase the coherence. Since the ERS-1/2 and ENVISAT IM2 descending have the same viewing geometry and the satellite paths are the same, these descending interferograms can be directly compared with each other for changes in the wavelength and location of the line-of-sight deformation. ERS-2 data after 2001 have inaccurate Doppler centroids, resulting in focusing problems and very few useful images for interferometry. We selected the same error-free ERS-2 images that Tizzani et al., (2015) processed during 2004-2009, but the data have very low coherence, resulting in very few coherent interferograms. Therefore ERS-2 data from 2004-2009 were not considered further.

ALOS-1 data

ALOS-1 data were processed with the NSBAS software with the same workflow as the ENVISAT data. We do not use ALOS-1 data between 2007-2010 due to its much lower sensitivity to subtle displacements of 2 cm/yr or less. Indeed, the caldera uplift and the subsidence at NGB that should be detected in 2007-2009 interferograms are not observed in many ALOS-1 pairs, even if they span almost 3 years. Several winter to winter pairs and interferograms that span different seasons of the year show strong double-bounce effects in wetlands. These effects are more problematic for L-band than C-band data. The ALOS-1 data for track 197 was chain stacked to span early 2010 to early 2011 when ENVISAT did not acquire data (Figure S2). We use a strong cascade sliding window filter for the interferograms with the double-bounce effects, but this is not able to cope with the phase discontinuities and tropospheric anomalies that cannot be completely corrected with the ERA-5 and empirical corrections. The stack of seven strict small baseline interferograms

records multiple unwrapping errors, double bounce signals and no clear evidence of caldera subsidence during February 2010 - February 2011 (Figure S5).

TerraSAR-X data

TerraSAR-X data were processed with the ISCE software following standard procedures, and with the 10 m USGS DEM to remove the topographic phase. Pixels were averaged 16 times prior to filtering and phase unwrapping and pixels below a coherence threshold of 0.35 were masked. Prior to the InSAR time series calculation, interferograms were referenced to a 100 by 100 pixel box in the few non-deforming areas (black crosses in Figure 2). We prefer this procedure instead of removing a ramp with an arbitrary offset due to the almost lack of non-deforming areas in the small TSX swaths. GPS deramping was not successful due to the small number of stations available during the time period – at most 4 per TSX track. Due to the small number of acquisitions during 2011 and 2012, and the near secular subsidence observed during this time period by the GPS data, we decided to stack the best interferograms that span this subsidence episode (2-6 per track). Atmospheric corrections were attempted with the North American Regional Reanalysis (NARR) and ERA-I atmospheric models implemented in the GIAnT toolbox (Jolivet et al., 2014), but the poor temporal resolution of these corrections imply that they do not significantly reduce the atmospheric phase delays. Hence, these interferograms were not corrected for atmospheric phase delays.

Text S3. Data inversion

Prior to source modeling, linear ramps were estimated in areas with no deformation and removed from the interferograms. The data were then downsampled with a resolution-based algorithm (Lohman and Simons, 2005) with a sill geometry at a depth of 15 km.

This source is only used to focus the downsampling in areas with deformation signals, with coarser downsampling in far-field areas with residual atmospheric phase delays (e.g., Fig. 7a-c in Lohman and Simons, 2005), and not to enforce a prior source model. Downsampling with a shallower sill does not result in a vastly different number of downsampled patches. We use a diagonal data covariance matrix for the InSAR data because the data have a very weak spatial correlation no bigger than a few downsampled pixels and because the far-field data standard deviation in non-deforming areas is $\sim$7 mm. Both GPS and InSAR data were weighted with the inverse of their uncertainties. For InSAR, this only takes into account the effect of the atmospheric phase delays that remain in the data after multiple corrections. Data were inverted with the neighborhood algorithm (Sambridge, 1999) (hereafter NA), a non-linear inversion method which iteratively searches for the best-fit model parameters avoiding local minima, and the Levenberg-Marquardt (LM) algorithm. Due to the vastly different amount of GPS and InSAR data points – 10 vs $\sim$2500 points, the GPS data should be weighted such that the InSAR data will not dominate the best-fit model. Hence, the GPS data were weighted with factors of 1, 0.2 and 0.1 to augment the relative weight of this data set with respect to InSAR and to test the optimal weighting for joint inversions (e.g., Fialko, 2004). Inversions with these weighting factors result in models that do not significantly differ from each other, fitting both the GPS and InSAR data equally well. Hence, both data sets are assigned equal weights in the non-linear inversion.

We invert the data in the following way. After the NA inversion converged resulting in models that do not significantly differ from each other, we use the best-fit NA model as the initial point of an inversion with the LM algorithm to find the global best-fit model.

Inversions for all 14 non-linear model parameters (X and Y sill centroid, depth, strike, dip, width, length) for the two sub-horizontal dislocations fail to converge to a stable family of solutions because the sources lie on top of each other and thereby have strong trade-offs. After several iterations we fix the dip and strike of the caldera source to 0^{o} and 54^{o} and the NGB source dip to 0^{o} because they converge rapidly to these values. Inversions for the rest of the 11 model parameters converge for the caldera source but not for the NGB source. At this point we discard models in which the NGB and the caldera sills intersect with each other. We then fix the 7 caldera source parameters and the NGB source centroid and depth, and invert for the NGB sill strike, length and width (Figure S6, Figure S7). This is similar to other studies where multiple deformation sources are iteratively determined (e.g., Bagnardi et al., 2013). Because we iteratively fixed the model parameters to ensure inversion convergence, it is neither feasible nor meaningful to calculate model parameter uncertainties. However, we calculate the source depths uncertainties with RMS plots in which all model parameters are fixed except for the sill centroid depths (Figure S8). To ensure that the model is robust, we also inverted the data with a different algorithm based on a non-linear least square iterative inversion (Tarantola and Valette, 1982), which gave very similar results. We use the best-fit caldera sill model as the starting point for an inversion for a sill and an ellipsoidal crack with the boundary element code DEFVOLC for the IM2 interferogram (Figure S9).

The distributed sill opening model is regularized with Laplacian smoothing to avoid unrealistic oscillatory opening and the amount of smoothing is chosen by the "L curve" corner (Aster et al., 2018). We jointly invert GPS and InSAR data with weighting factors α_W between 1 (equal weight for GPS and InSAR), 0.5 and 0.2 to augment the GPS con-

tribution with respect to InSAR. The model fit to the GPS data improves with $\alpha_W = 0.5$ at the expense of a worst data fit to the InSAR data near NGB. Smaller values of α_W result in a near complete fit to the GPS data but higher residuals for the InSAR data. Therefore, we invert the data with $\alpha_W = 0.5$ which provides good data fits without significantly increasing the residual for the NGB signal recorded by the interferograms (Figure 4-5, Figure S10).

Text S4. Solution to the equations of pressure change for the caldera and NGB sills

Magma compressibility

For the general case of volume change due to a pressure change in a reservoir (Equation 1)

$$\Delta P_{s,d} = \frac{\Delta V_{s,d}}{V_{s,d}(\beta_m + \beta_w)} \tag{1}$$

with V the reservoir volume, β_m the magma compressibility and β_w the reservoir compressibility, equal to $\frac{3}{4G}$ for a sphere and $\frac{8(1-\nu)}{3\pi}\frac{a_{s,d}^3}{G}\frac{1}{V}$ for a penny-shaped crack (Amoruso and Crescentini, 2009). This results in the Equation 2

$$\Delta V_{s,d} = \Delta P_{s,d}(\frac{\pi a_{s,d}^3 \gamma}{G} + V_{s,d}\beta_m) \tag{2}$$

If magma compressibility is taken into account, then the time constants in Equation 10 become

$$\begin{aligned}\beta &= \frac{\pi a_2^4 G}{8\mu_2 H_2(\pi a_s^3\gamma + GV_s\beta_m)} \\ \alpha &= \frac{\pi a^4 G}{8\mu H(\pi a_s^3\gamma + GV_s\beta_m)} \\ \epsilon &= \frac{\pi a_2^4 G}{8\mu_2 H_2(\pi a_d^3\gamma + GV_d\beta_m)}\end{aligned} \tag{3}$$

Method of solution

Rearranging terms results in Equations 8-9 in the main text

$$\frac{d\Delta P_s}{dt} = -\Delta P_s(\alpha+\beta) + \Delta P_d\beta + \alpha(\Delta\bar{P} + \Delta\rho g H) + \beta\Delta\rho_2 g H_2 \tag{4}$$

$$\frac{d\Delta P_d}{dt} = \Delta P_s\epsilon - \Delta P_d\epsilon - \epsilon\Delta\rho_2 g H_2 \tag{5}$$

Equation 4 - Equation 5 form a linear system of non-homogeneous differential equations that can be casted in matrix form (Equation 6 - Equation 7)

$$\begin{bmatrix}\frac{d\Delta P_s}{dt} \\ \frac{d\Delta P_d}{dt}\end{bmatrix} = \begin{bmatrix}-\alpha-\beta & \beta \\ \epsilon & -\epsilon\end{bmatrix}\begin{bmatrix}\Delta P_s \\ \Delta P_d\end{bmatrix} + \begin{bmatrix}\beta\Delta\rho_2 g H_2 + \alpha\Delta\rho g H + \alpha\Delta\bar{P} \\ -\epsilon\Delta\rho_2 g H_2\end{bmatrix} \tag{6}$$

$$\frac{d\bar{P}}{dt} = G\bar{P} + H \tag{7}$$

with $\bar{P} = [\Delta P_s, \Delta P_d]^T$ the vector that contains the functions for the shallow and deep reservoir pressure. The solution to Equation 7 is a function of the form $\vec{\bar{P}}(t) = \vec{v_1}e^{\lambda_1 t} + \vec{v_2}e^{\lambda_2 t} + \vec{a}e^{-\frac{t}{\tau_m}} + \vec{b}$ with $\vec{v_{1,2}}$ and $\lambda_{1,2}$ the eigenvectors and eigenvalues of G, and the last two terms are vectors derived from the method of undetermined coefficients for the non-homogeneous terms (last term on the right-hand side of Equation 7).

Figures

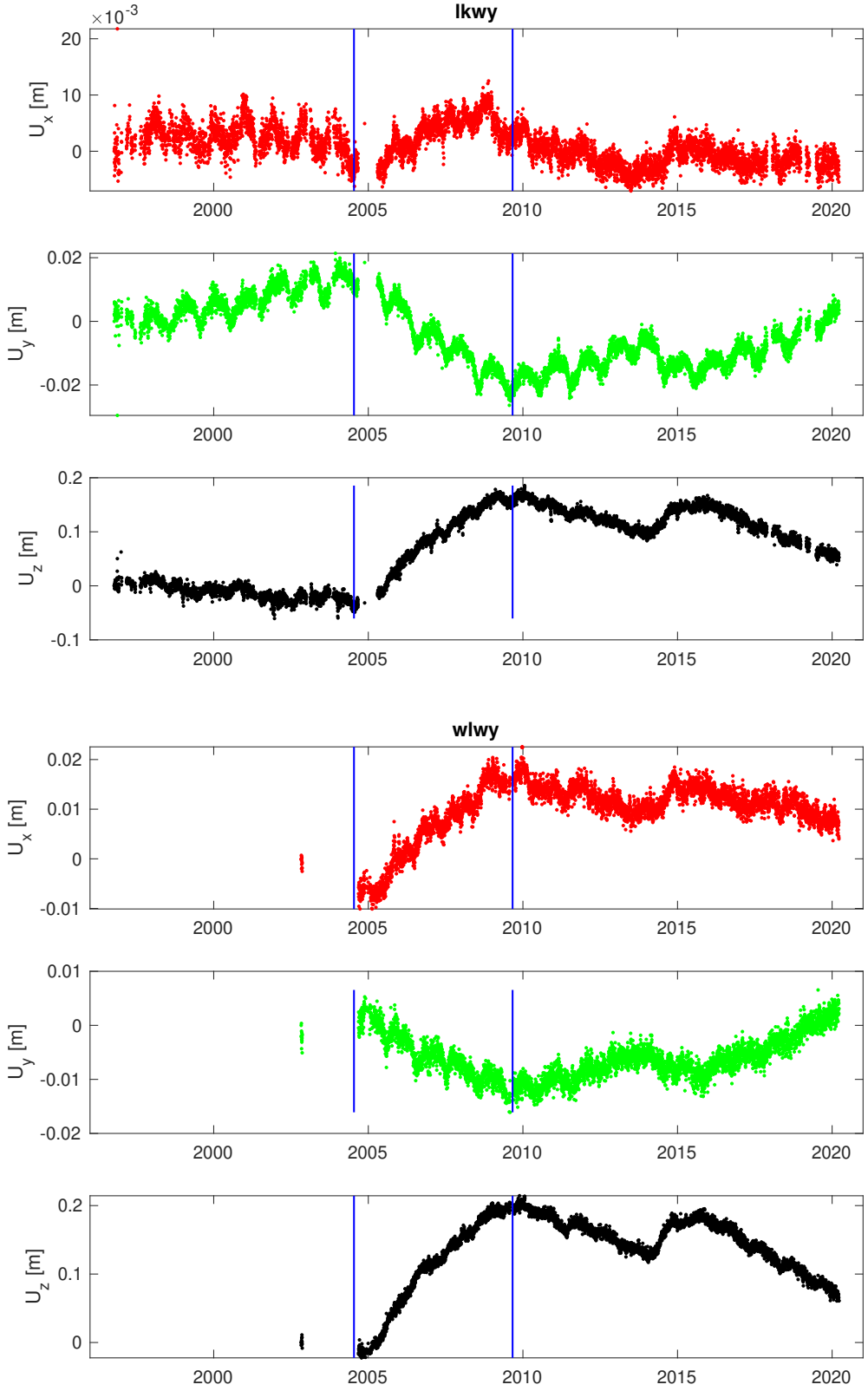

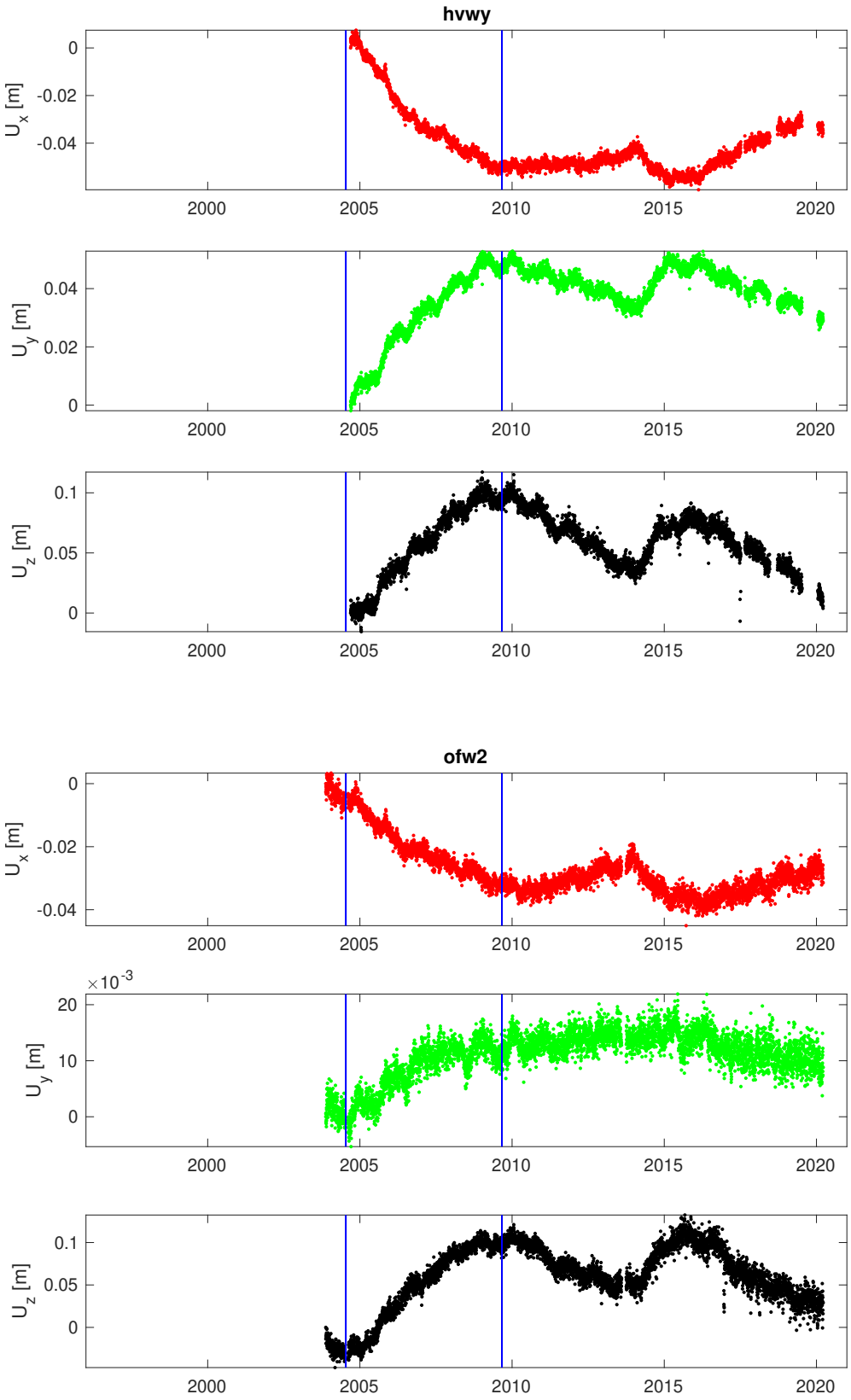
hvwy
U_x [m]
0
-0.02
-0.04
2000
2005
2010
2015
2020
U_y [m]
0.04
0.02
0
U_z [m]
0.1
0.05
ofw2
×10^-3
20
10

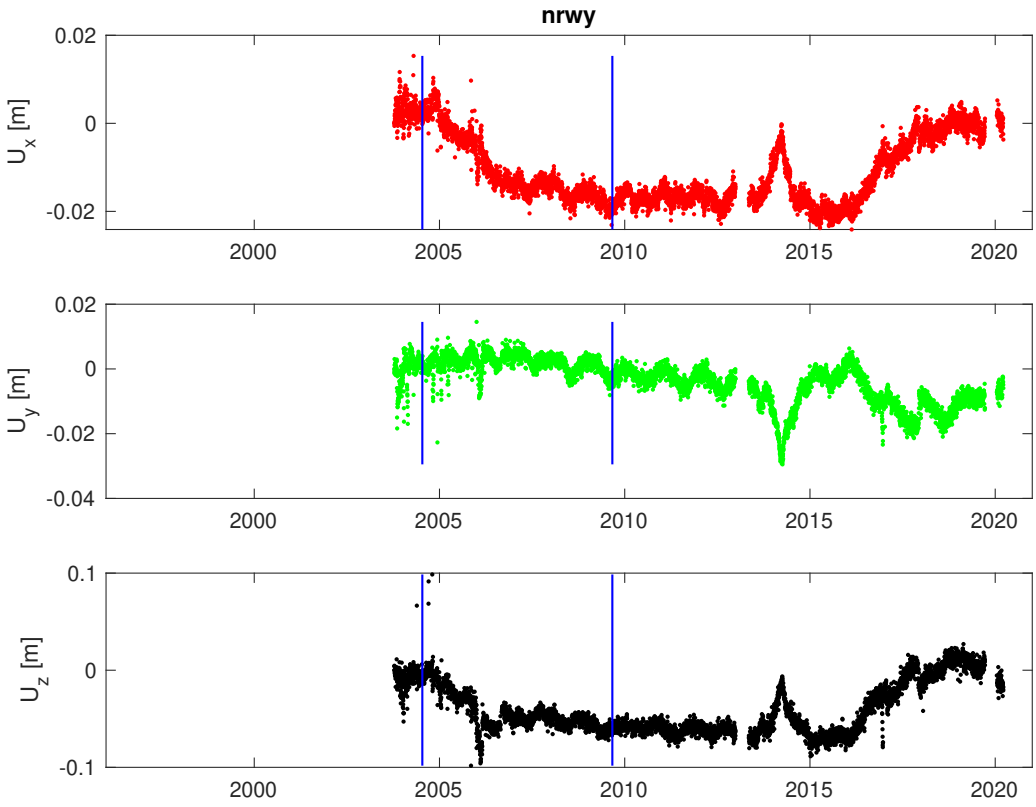

Figure S1: Continuous GPS time series for east (U_x), north (U_y) and vertical (U_z) components. The figure title shows the station name. Vertical blue lines show the 2004-2009 episode of uplift for which positions were averaged on windows of +/-10 days and subtracted to retrieve the total displacement for each component.

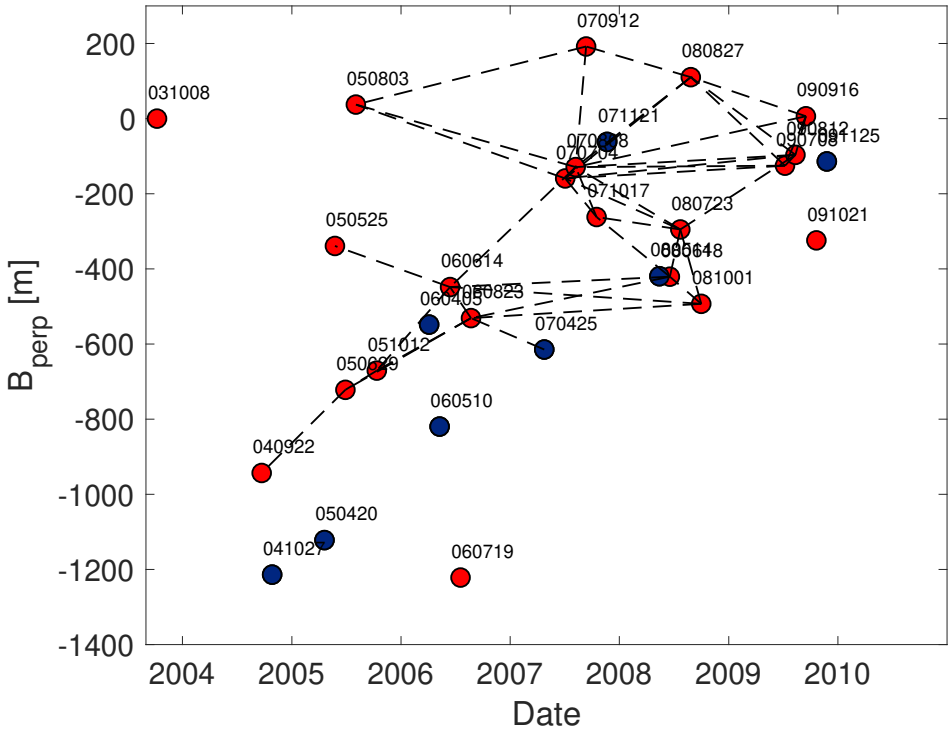

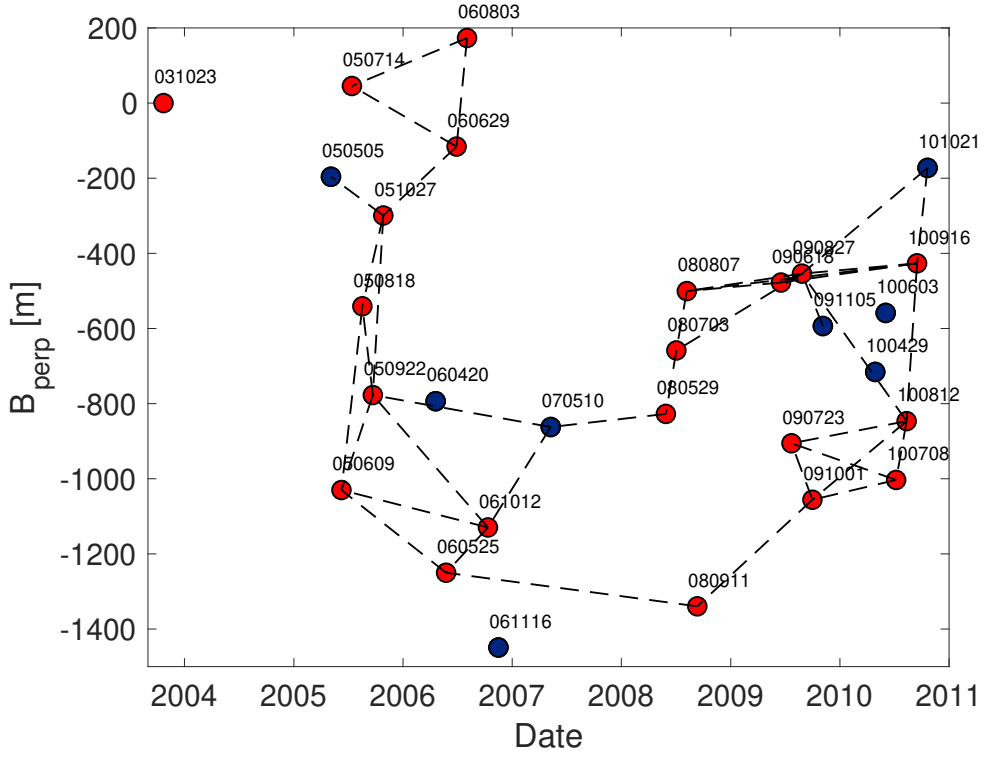
060803
050714
031023
060629
050505
101021
051027
090827
100916
080807
090618
050818
100603
091105
080703
100429
050922
060420
080529
100812
070510
090723
050609
100708
091001
061012
060525
080911
061116
200
0
-200
-400
-600
-800
-1000
-1200
-1400
B perp [m]
2004
2005
2006
2007
2008
2009
2010
2011
Date

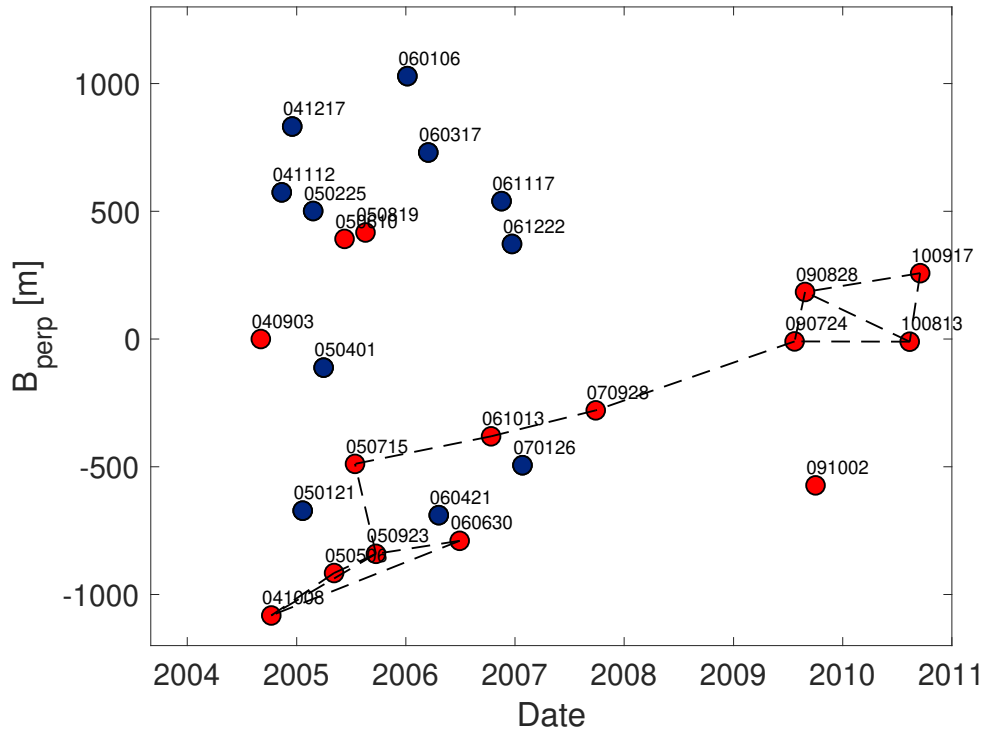
060106
041217
060317
041112
050225
061117
050819
061222
100917
090828
040903
090724
100813
050401
070928
061013
050715
070126
091002
050121
060421
060630
050923
041008
1000
500
0
-500
-1000
B perp [m]
2004
2005
2006
2007
2008
2009
2010
2011
Date

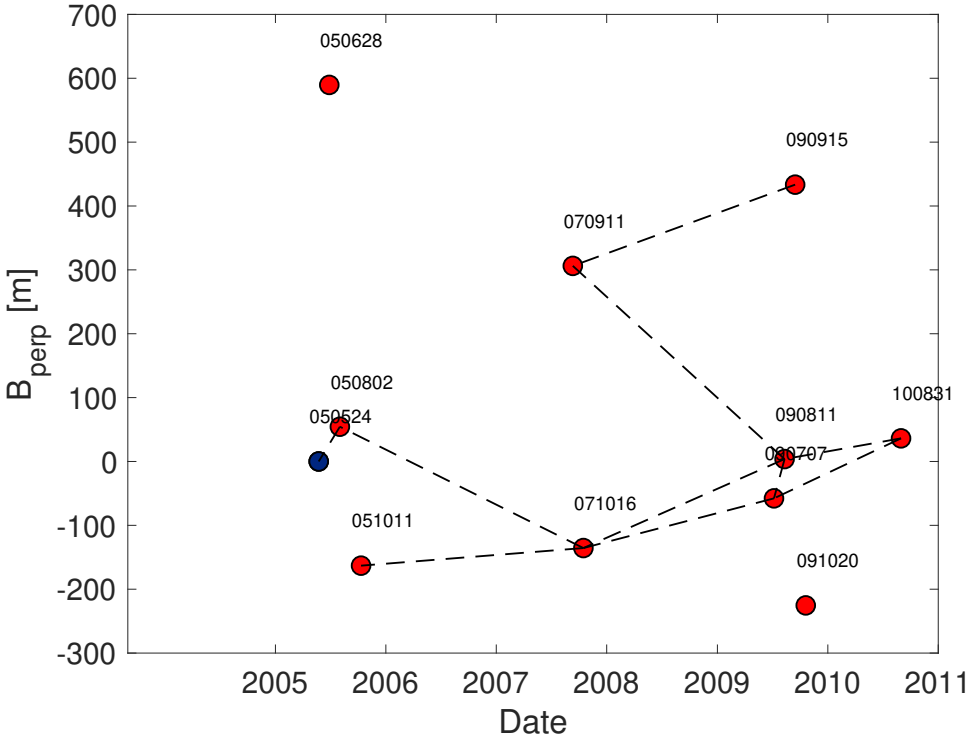
700
600
500
400
300
200
100
0
-100
-200
-300
B perp [m]
2005
2006
2007
2008
2009
2010
2011
Date
050628
090915
070911
050802
050524
090811
100831
090707
071016
051011
091020

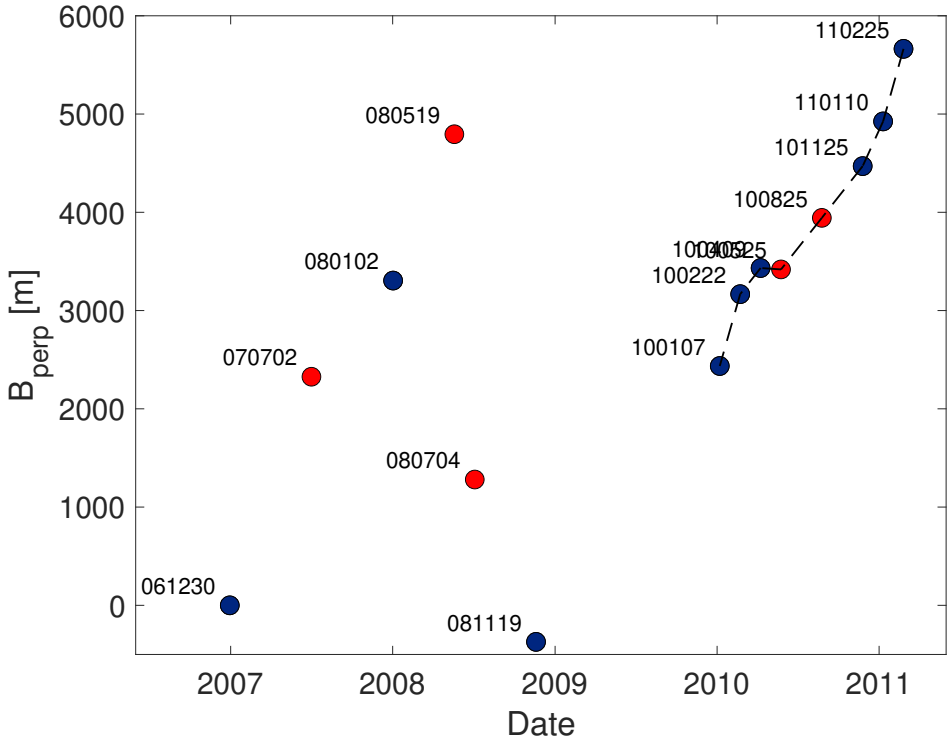
6000
5000
4000
3000
2000
1000
0
B perp [m]
2007
2008
2009
2010
2011
Date
110225
080519
110110
101125
100825
080102
100222
070702
100107
080704
061230
081119

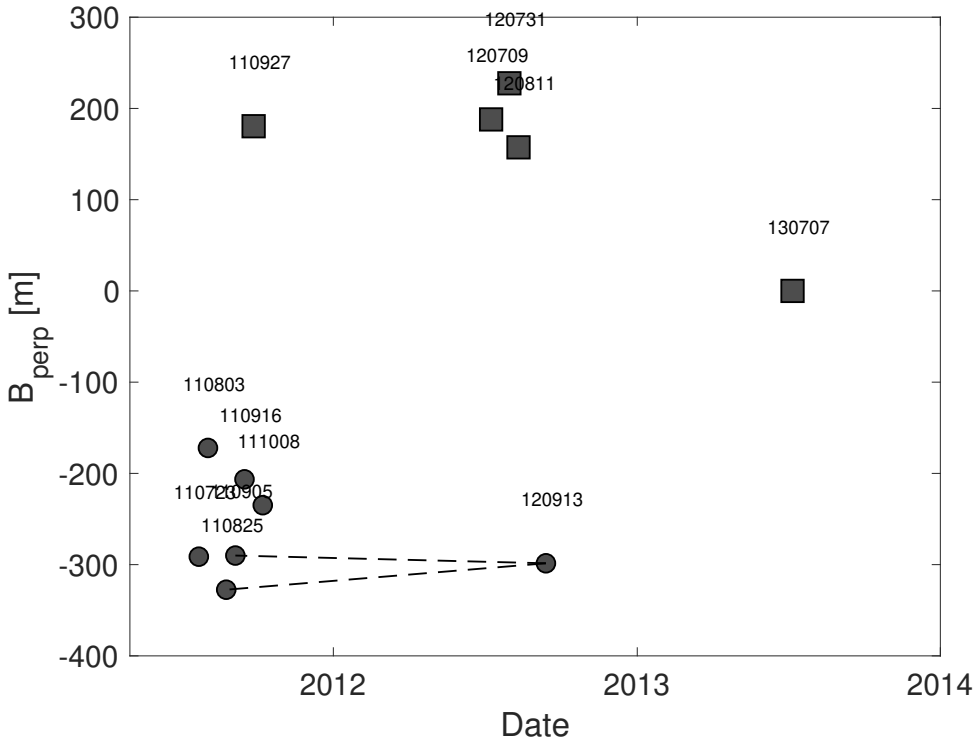
300
200
100
0
-100
-200
-300
-400
B perp [m]
2012
2013
2014
Date
120731
110927
120709
120811
130707
110803
110916
111008
110825
120913

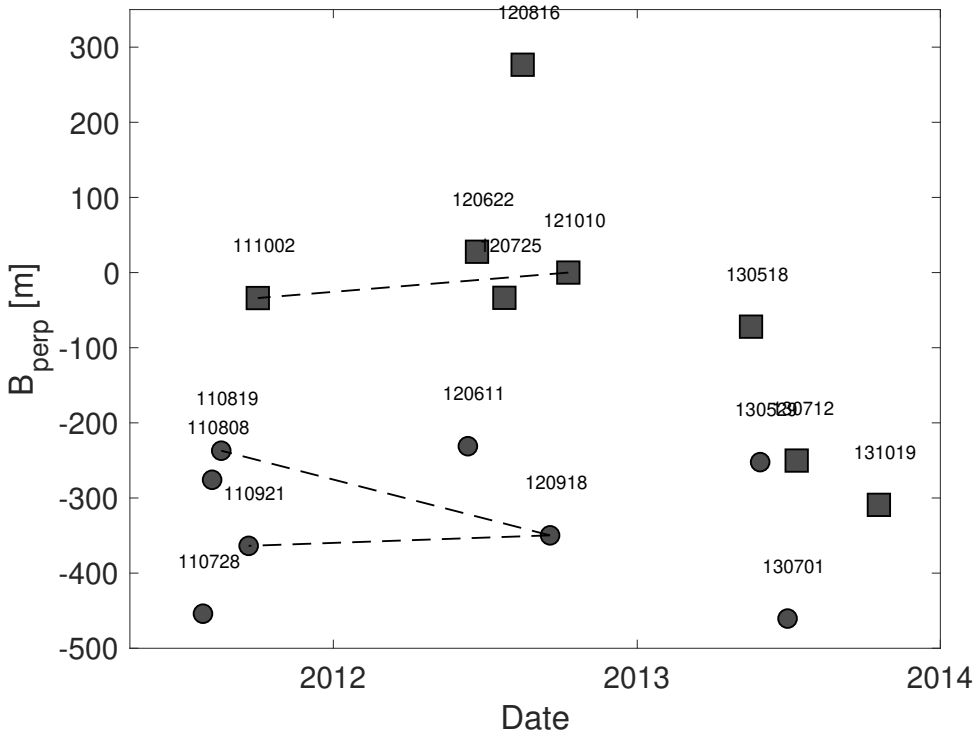
300
200
100
0
-100
-200
-300
-400
-500
B perp [m]
2012
2013
2014
Date
120816
120622
121010
111002
120725
130518
110819
120611
110808
120918
131019
110921
110728
130701

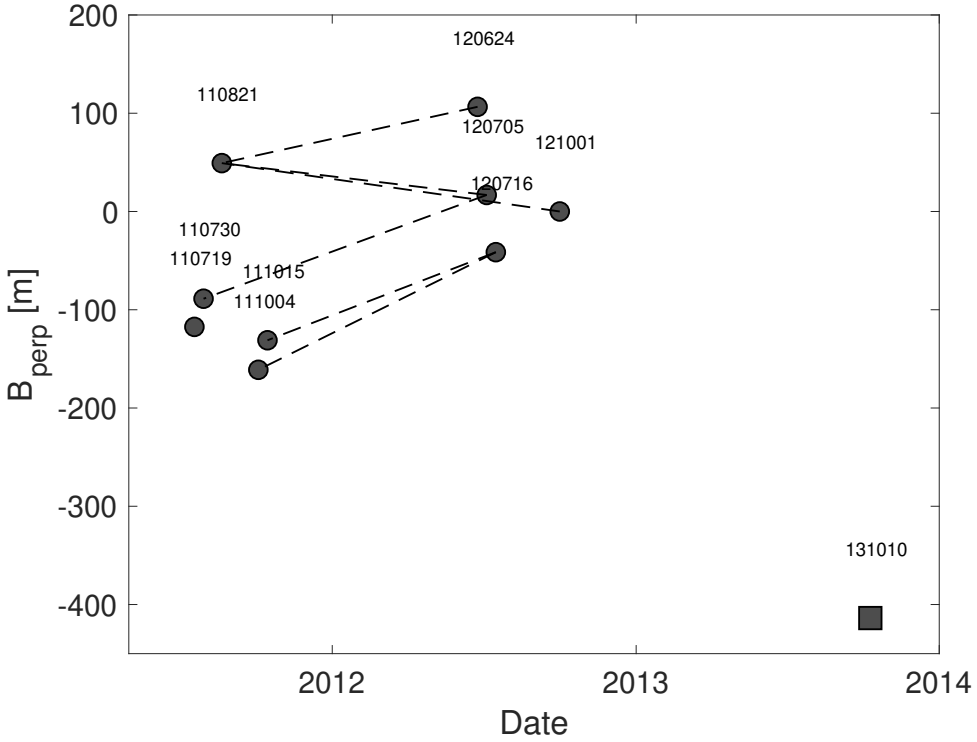

Figure S2: B_{perp} plot for ENVISAT (a IM2 ascending track 320, b IM2 descending track 48, c IM1 ascending track 48, d IM1 descending track 31), ALOS-1 (e ascending path 197) and TerraSAR-X/TanDEM-X data (f ascending orbit 45, g ascending orbit 121, h descending orbit 159). Red and blue dots are winter and non-winter images for the ENVISAT and ALOS-1 data. Winter images were not included in the B_{perp}plot for the ENVISAT descending tracks. Circles and squares are TerraSAR-X and TanDEM-X images.

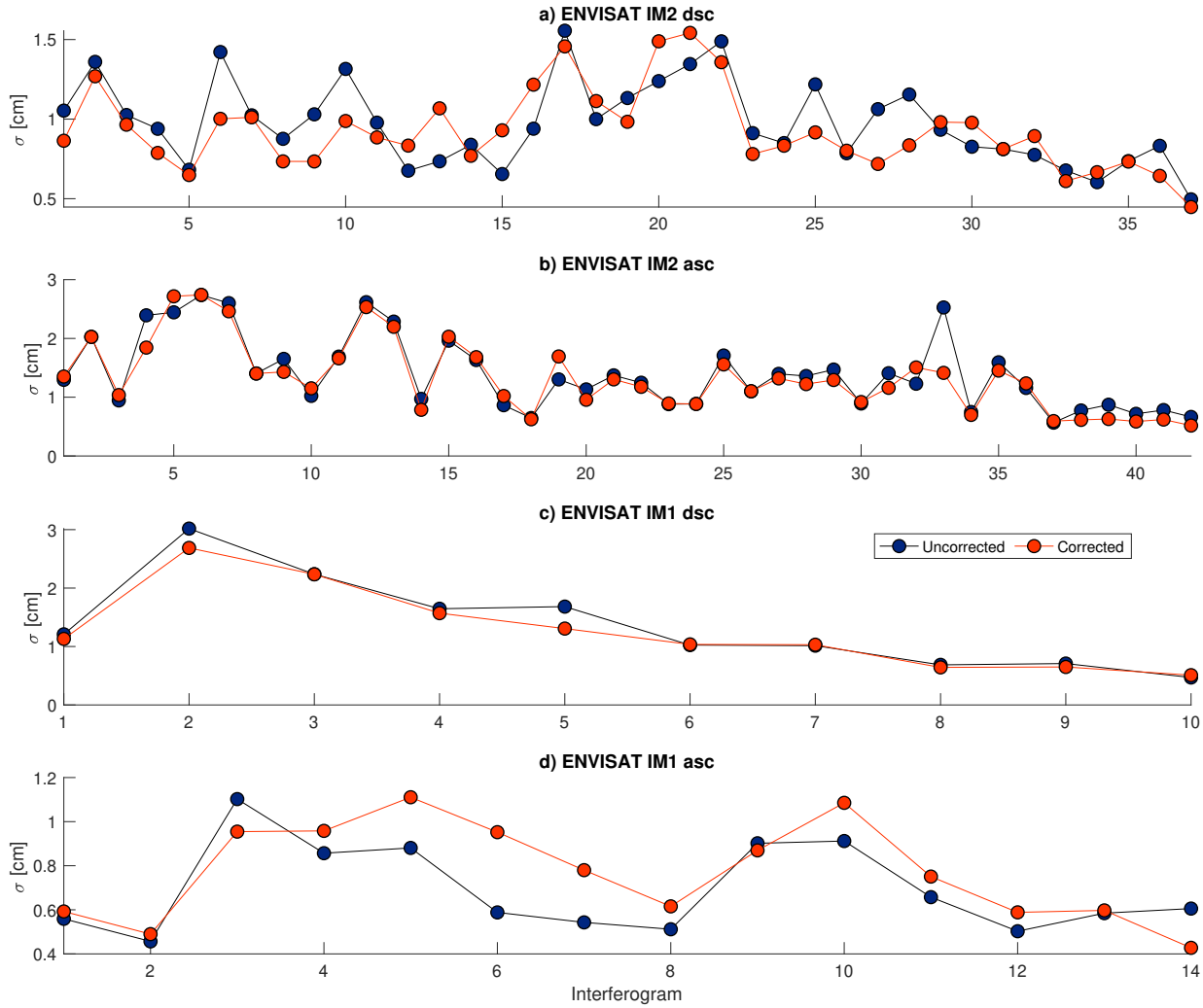

Figure S3: Statistics of atmospheric phase delays for the interferograms used in each of the ENVISAT time series. The title shows the ENVISAT track. The blue and orange circles are the standard deviation in non-deforming areas uncorrected and corrected with the ERA5 atmospheric model. The figure shows that ERA5 reduces the data standard deviation in more than half of the interferograms per track except for the ENVISAT IM1. Therefore this track was not corrected with ERA5.

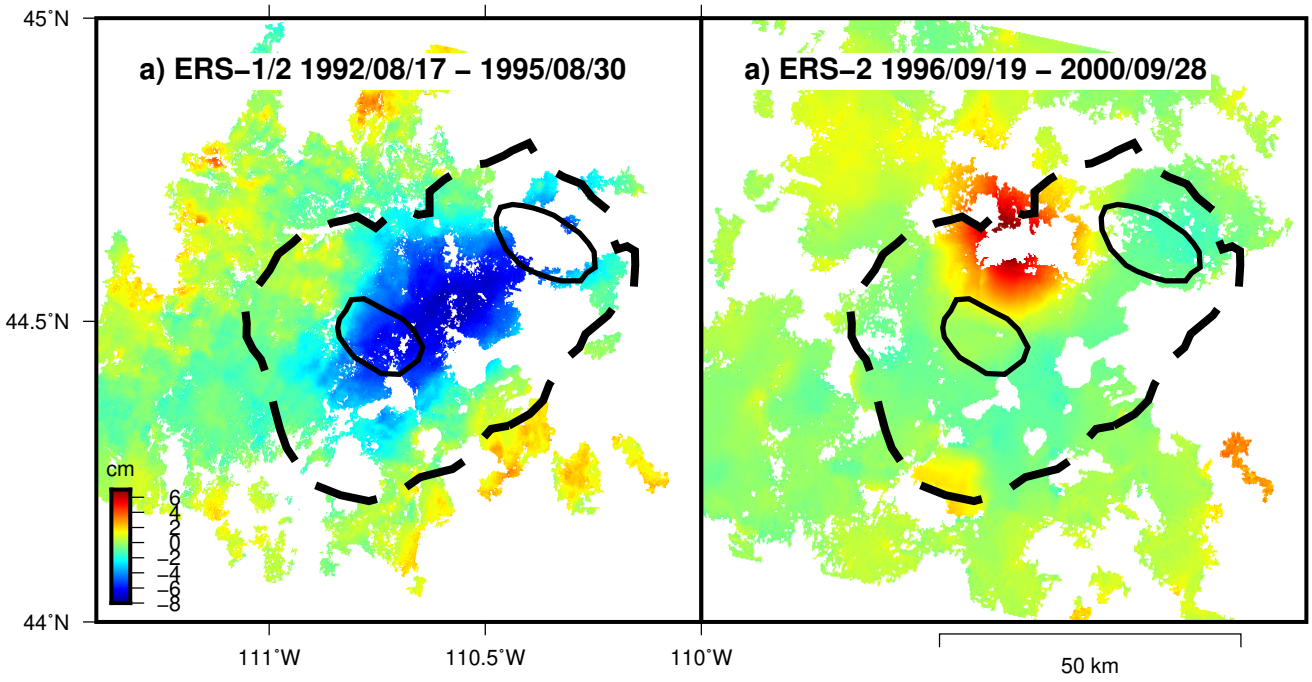

Figure S4: ERS-1/2 interferograms recorded between 1992 and 2000. A) Stack of two interferograms that spans 1992/08/17 - 1993/06/28 and 1993/06/28 - 1995/08/30 showing caldera subsidence (Wicks et al., 1998, Aly and Cochran, 2011) in a different location than uplift during 2004-2009 and subsidence during 2010-2012. B) Interferogram that spans 1996/09/19 - 2000/09/28 showing uplift at NGB (Wicks et al., 2006, Aly and Cochran, 2011) but in a different location than the subsidence during 2004-2009. The data are not modeled and only shown for visual comparison with the ENVISAT interferograms (Figure 2).

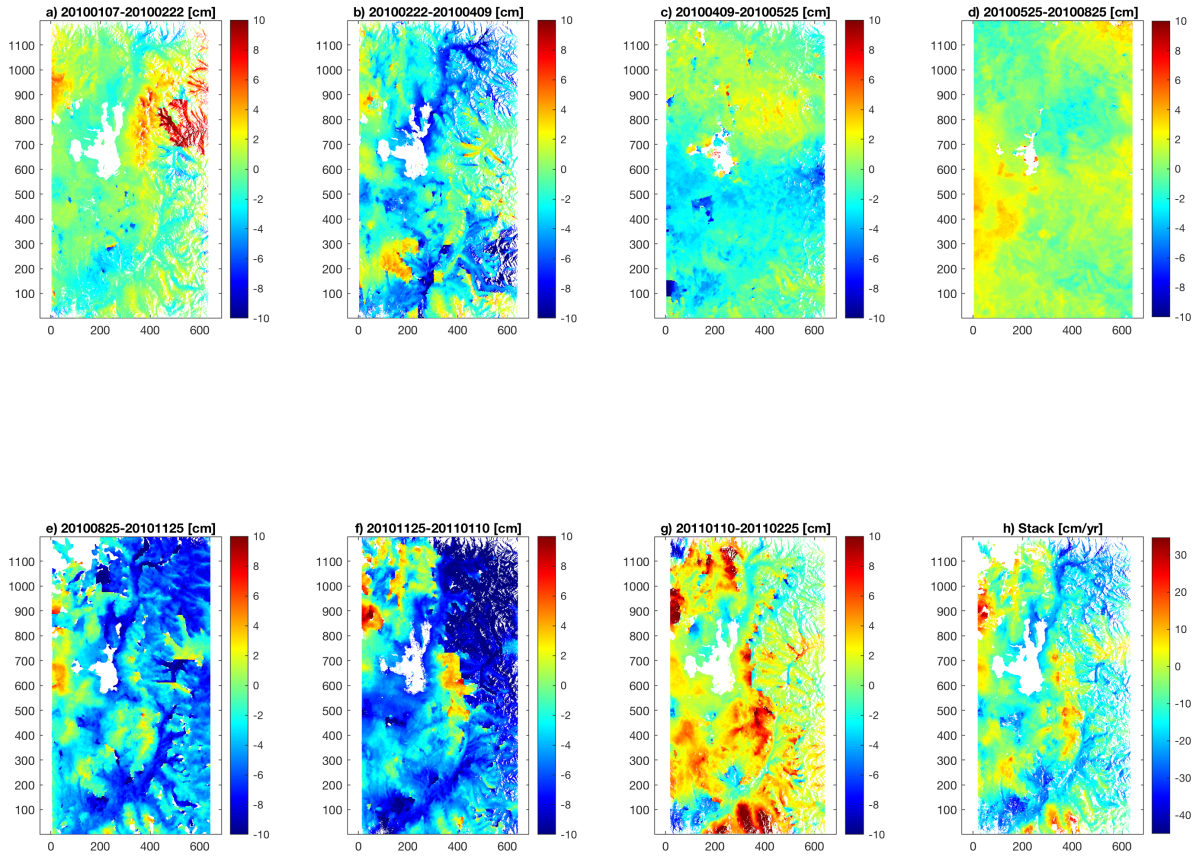

Figure S5: a-g) ALOS-1 interferograms in radar coordinates that span 46-92 days between January 2010 and February 2011 (Figure S2e). The titles show the date span of each interferogram. The data show several double bounce signals and unwrapping errors due to topography correlated phase delays that cannot be corrected with a linear function that correlates phase and topography. h) Mean ground velocity in the LOS direction calculated by stacking the preceding interferograms.

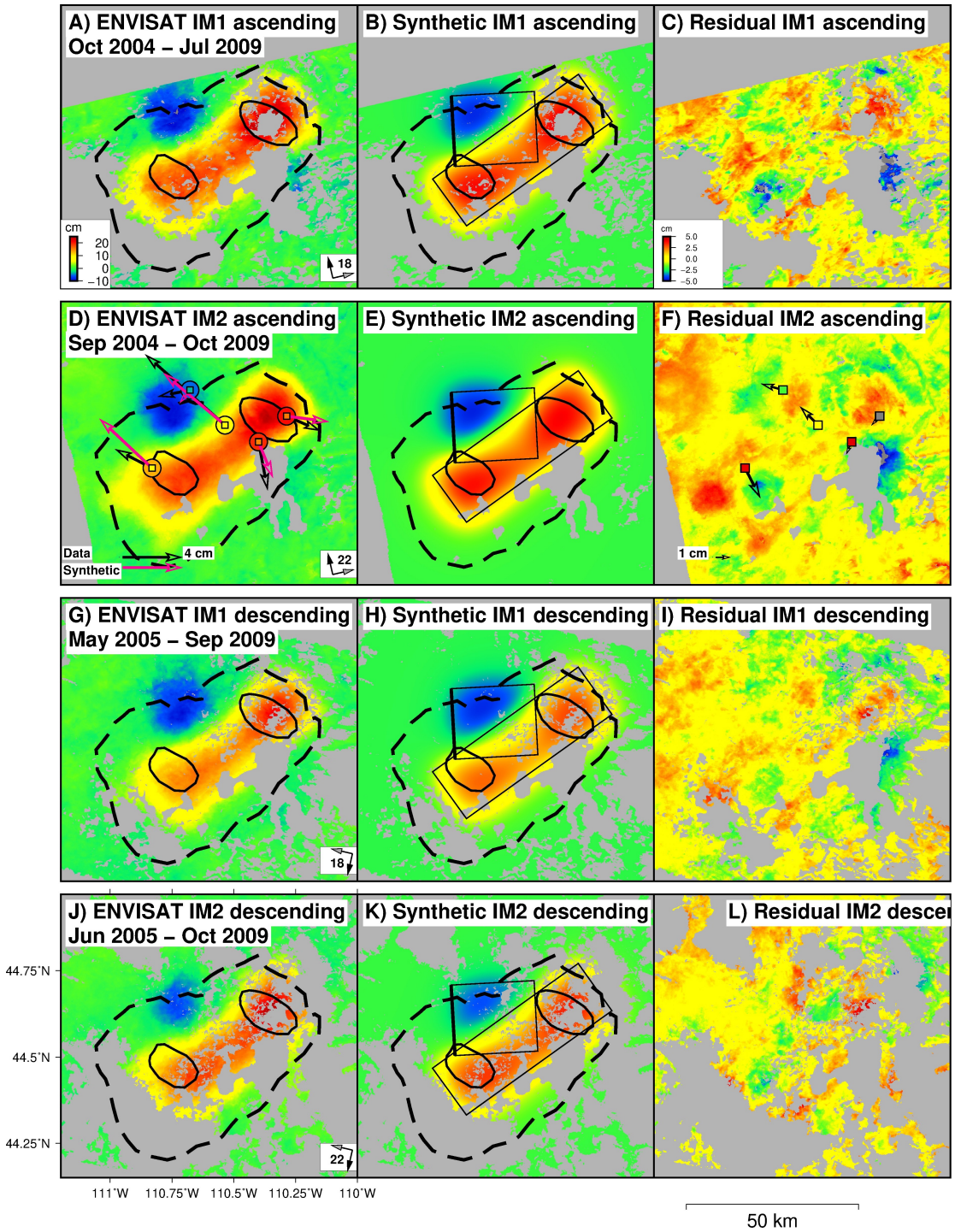

Figure S6: Interferograms (A,D,G,J), synthetic interferograms and GPS vectors (B,E,H,K), and residuals (C,F,I,L) for the ENVISAT interferograms for the inversion of two sub-horizontal dislocations with uniform opening. The black and pink arrows show the GPS vectors (Figure S1) and predicted displacement by best-fit sill models (black rectangles in E-H). The dots and squares in B show the GPS vertical displacement and synthetic displacements. The vertical component was not included in the inversion because they are less accurate than the horizontal components. Hence we only calculate the synthetic vertical displacement from the best-fit source model and subtract it from the data.

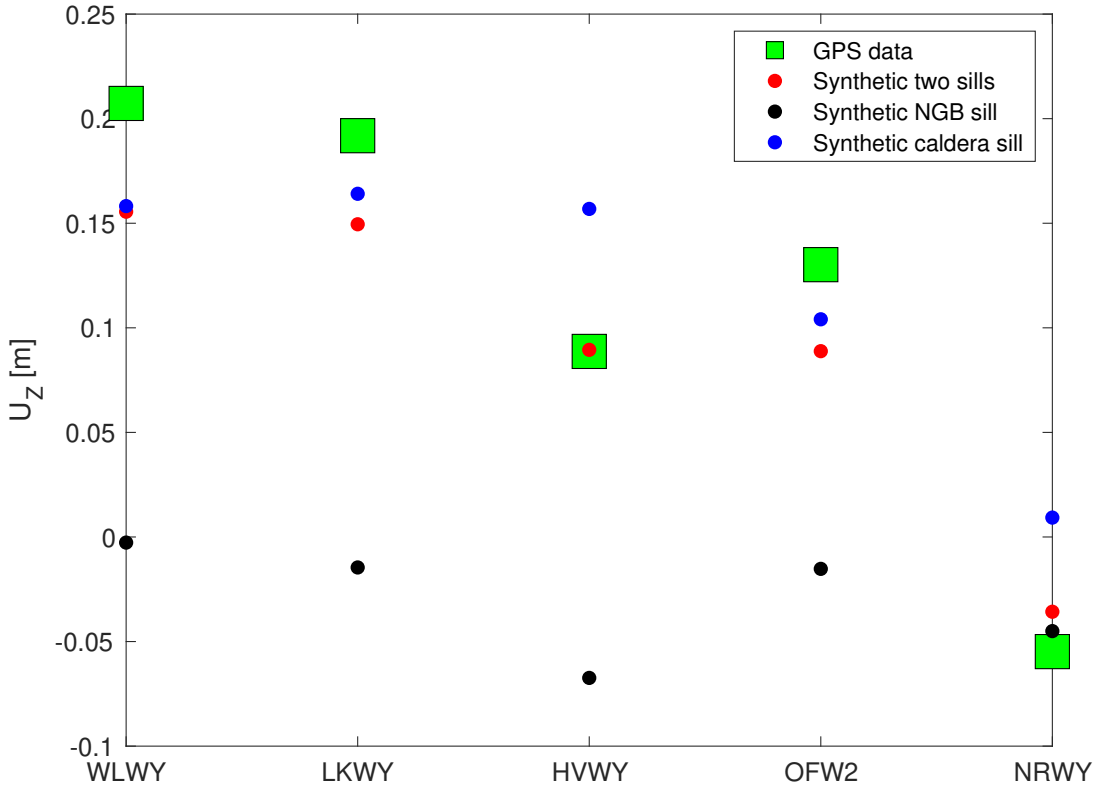

Figure S7: GPS vertical displacement (green squares) and displacement predicted by the best-fit model of two sills with uniform opening (dots). The blue and black circles show the synthetic displacement predicted by the caldera and NGB sources with uniform opening. The red dots show the synthetic vertical displacement predicted by the two sills. The figure shows that the vertical displacements measured by stations WLWY, LKWY and OFW2 are almost completely modeled by the opening of the caldera source. Therefore the GPS time series vertical displacement of these stations are sensitive to the caldera sill opening. The misfits of ∼5 cm with respect to the GPS data show that distributed opening is required to model the data due to localized uplift at SCD and MLD.

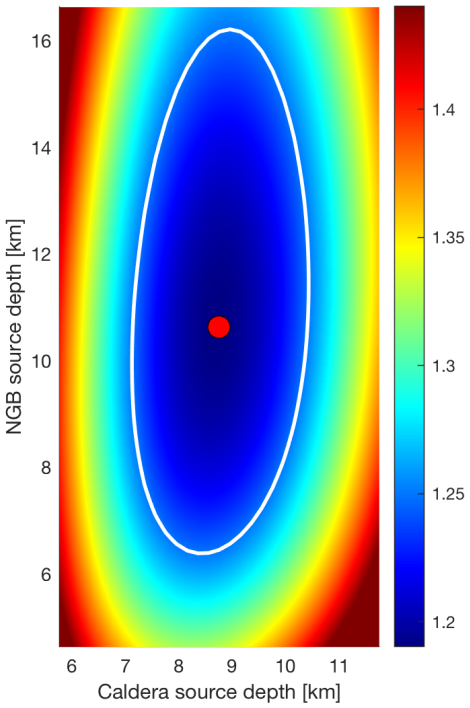

Figure S8: Root mean square (RMS) trade-off plot in cm for the caldera and NGB sill sources depths. The red dot is the RMS global minimum. The white line is the 5% contour above the global minimum and is used as a proxy for the sources depth uncertainties. Since the sources cannot intersect with each other, the NGB source depth uncertainty is much narrower than the prediction of the RMS white contour.

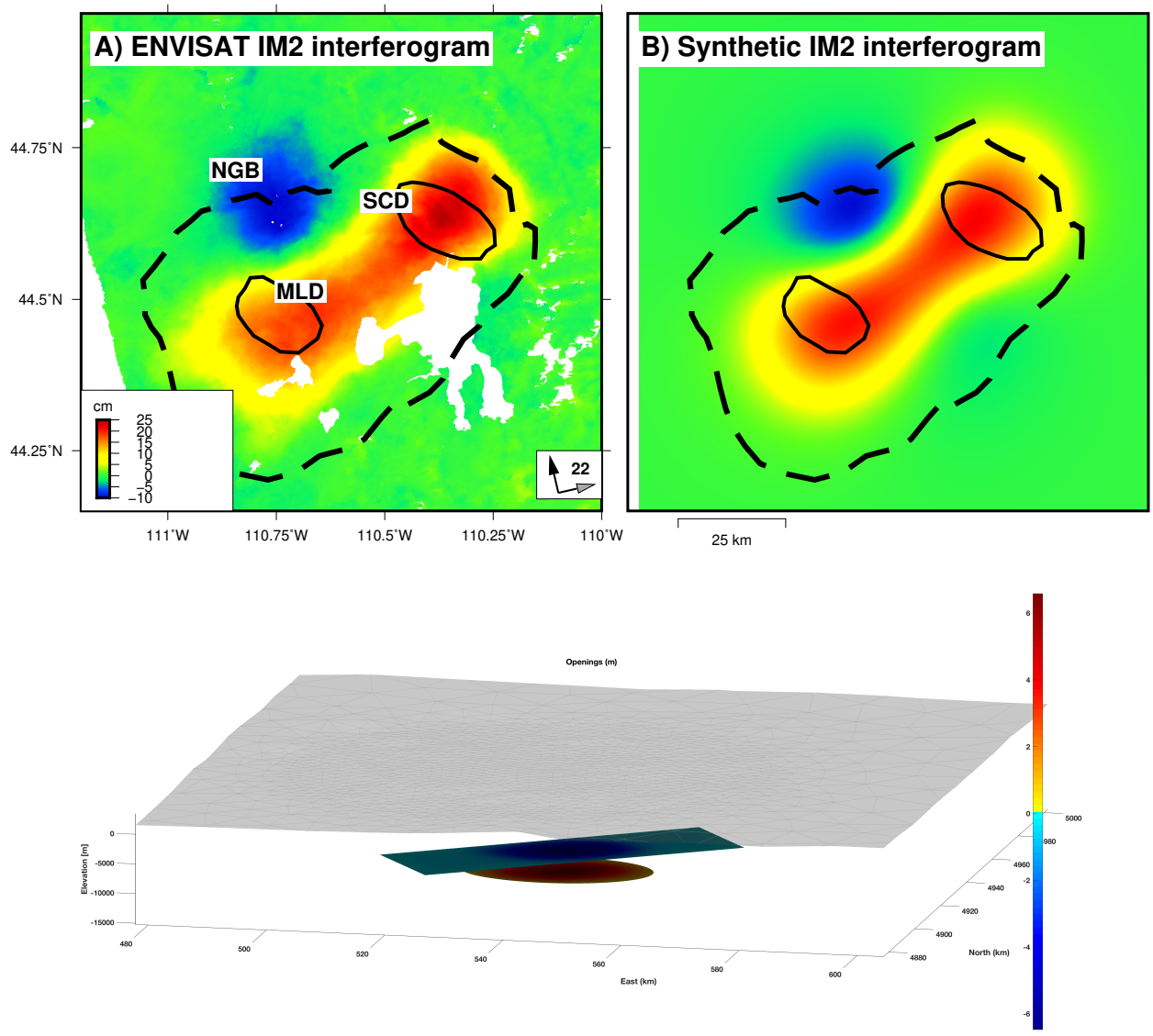

Figure S9: Boundary element model. Top. IM2 ascending ENVISAT interferogram (A), synthetic interferogram (B). Bottom. Perspective view of the boundary element caldera sill and NGB ellipsoid. Positive colors show ellipsoid closing and negative colors show sill opening.

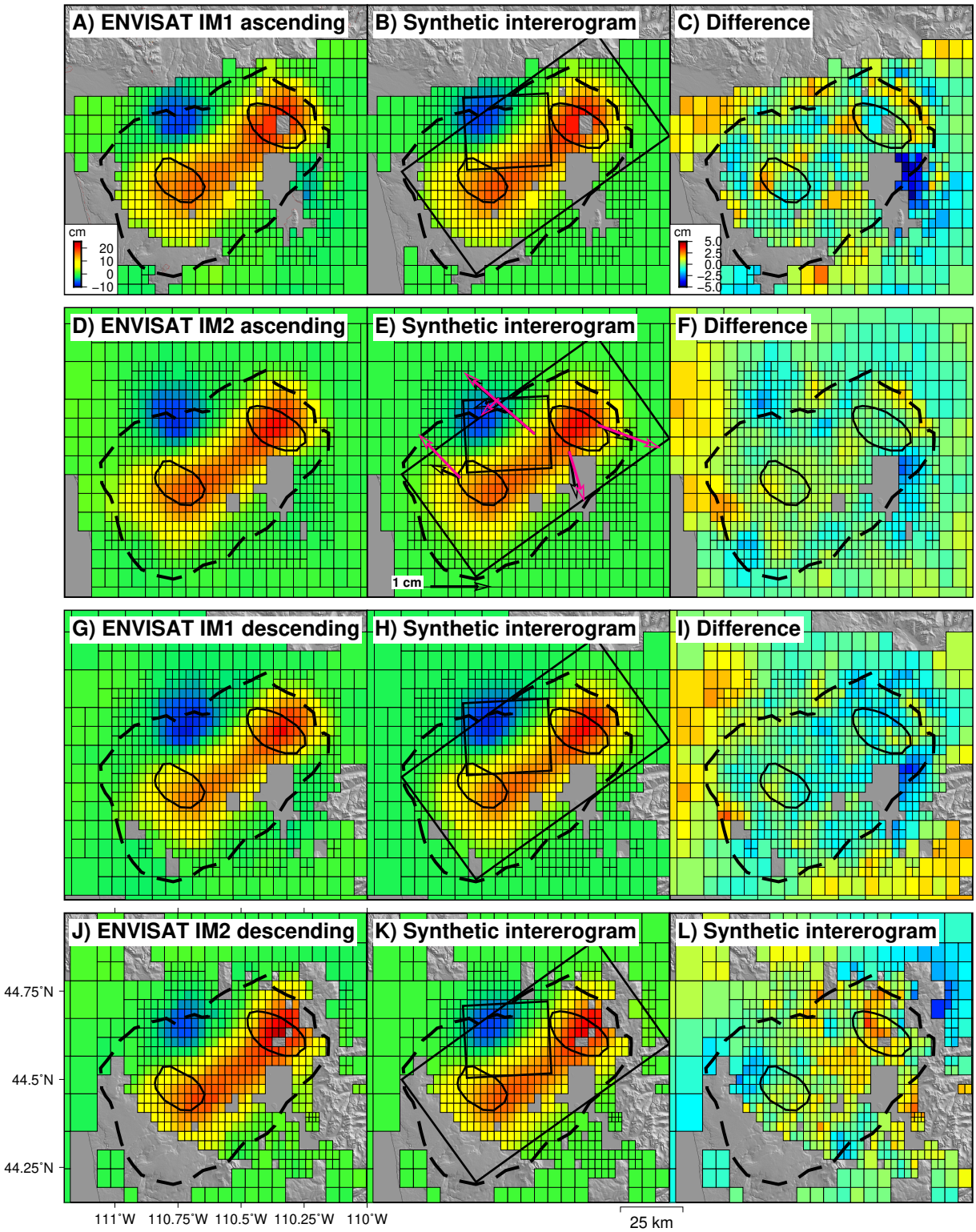

Figure S10: ENVISAT interferograms (A,D,G,J), synthetic data (B,E,H,K) and residuals (C,F,I,L) for the inversion of two sub-horizontal dislocations with distributed opening during 2005-2009 (Figure 5B). The black and pink arrows in E show the GPS vectors and predicted displacement by best-fit sill models.